

18. The International HapMap Consortium, *Nature* **426**, 789 (2003).
19. A. R. Templeton, E. Boerwinkle, C. F. Sing, *Genetics* **117**, 343 (1987).
20. D. W. Schultz *et al.*, *Hum. Mol. Genet.* **12**, 3315 (2003).
21. M. Hayashi *et al.*, *Ophthalmic Genet.* **25**, 111 (2004).
22. G. J. McKay *et al.*, *Mol. Vis.* **10**, 682 (2004).
23. S. Rodríguez de Córdoba, J. Esparza-Gordillo, E. Goicoechea de Jorge, M. Lopez-Trascasa, P. Sanchez-Corral, *Mol. Immunol.* **41**, 355 (2004).
24. L. V. Johnson, W. P. Leitner, M. K. Staples, D. H. Anderson, *Exp. Eye Res.* **73**, 887 (2001).
25. R. F. Mullins, S. R. Russell, D. H. Anderson, G. S. Hageman, *FASEB J.* **14**, 835 (2000).
26. J. Ambati *et al.*, *Nat. Med.* **9**, 1390 (2003).
27. G. S. Hageman *et al.*, *Prog. Retinal Eye Res.* **20**, 705 (2001).
28. J. Esparza-Gordillo *et al.*, *Immunogenetics* **56**, 77 (2004).
29. G. Wistow *et al.*, *Mol. Vis.* **8**, 205 (2002).
30. R. F. Mullins, N. Aptsiauri, G. S. Hageman, *Eye* **15**, 390 (2001).
31. A. M. Blom, L. Kask, B. Ramesh, A. Hillarp, *Arch. Biochem. Biophys.* **418**, 108 (2003).
32. J. M. Seddon, G. Gensler, R. C. Milton, M. L. Klein, N. Rifai, *JAMA* **291**, 704 (2004).
33. The Raymond and Beverly Sackler Fund for Arts and Sciences' generous support made this project possible. We thank Raymond Sackler, J. Sackler, and E. Vosburg for their input and encouragement. We also thank AREDS participants and investigators; G. Gensler, T. Clemons, and A. Lindblad for work on the AREDS Genetic Repository; S. Westman and A. Evan for assistance with the microarrays; R. Fariss for the human retinal sections and advice on confocal microscopy; E. Johnson for assistance with immunostaining; and J. Majewski for constructive comments on the manuscript. Partially funded by NIH-K25HG000060 and

NIH-R01EY015771 (J.H.), Macula Vision Research Foundation and the David Woods Kemper Memorial Foundation (C.B.), NIH-R01MH44292 (J.O.), and NIH-K01RR16090 and Yale Pepper Center for Study of Diseases in Aging (C.Z.). This work also benefited from the International HapMap Consortium making their data available prior to publication.

**Supporting Online Material**  
www.sciencemag.org/cgi/content/full/1109557/DC1  
Materials and Methods  
Fig. S1  
Tables S1 to S5  
References

10 January 2005; accepted 22 February 2005  
Published online 10 March 2005;  
10.1126/science.1109557

Include this information when citing this paper.

## REPORTS

superconductors. However, these materials are rather complex and do not easily lend themselves to a universal understanding of QPTs. To this end, it is desirable to identify quantum critical systems with a well-defined and solvable Hamiltonian and with a precisely controllable tuning parameter. One very simple model displaying a QPT is the Ising ferromagnet in a transverse magnetic field (5, 7–9) with the Hamiltonian

$$\mathcal{H} = -\sum_{ij} J_{ij} \sigma_i^z \cdot \sigma_j^z - \Gamma \sum_i \sigma_i^x \quad (1)$$

where  $J_{ij}$  is the coupling between the spins on sites  $i$  and  $j$  represented by the Pauli matrices  $\sigma^z$  with eigenvalues  $\pm 1$ . In the absence of a magnetic field, the system orders ferromagnetically below a critical temperature  $T_c$ . The transverse-field  $\Gamma$  mixes the two states and leads to destruction of long-range order in a QPT at a critical field  $\Gamma_c$ , even at zero temperature. In the ferromagnetic state at zero field and temperature, the excitation spectrum is momentum independent and is centered at the energy  $4\sum_j J_{ij}$  associated with single-spin reversal. Upon application of a magnetic field, however, the excitations acquire a dispersion, softening to zero at the zone center  $q = 0$  when the QPT is reached.

We investigated the excitation spectrum around the QPT in  $\text{LiHoF}_4$ , which is an excellent physical realization of the transverse-field Ising model, with an added term accounting for the hyperfine coupling between electronic and nuclear moments (10–12). The dilution series  $\text{LiHo}_x\text{Y}_{1-x}\text{F}_4$  is the host for a wide variety of collective quantum effects, ranging from tunneling of single moments and domain walls to quantum annealing, entanglement, and Rabi oscillations (13–17). These intriguing properties rely largely on the ability of a transverse field, whether applied externally or generated internally by the off-diagonal part of the magnetic dipolar interaction, to mix two degenerate crystal field states of each Ho ion.

## Quantum Phase Transition of a Magnet in a Spin Bath

H. M. Rønnow,<sup>1,2,3\*</sup> R. Parthasarathy,<sup>2</sup> J. Jensen,<sup>4</sup> G. Aeppli,<sup>5</sup>  
T. F. Rosenbaum,<sup>2</sup> D. F. McMorrow<sup>3,4,6</sup>

The excitation spectrum of a model magnetic system,  $\text{LiHoF}_4$ , was studied with the use of neutron spectroscopy as the system was tuned to its quantum critical point by an applied magnetic field. The electronic mode softening expected for a quantum phase transition was forestalled by hyperfine coupling to the nuclear spins. We found that interactions with the nuclear spin bath controlled the length scale over which the excitations could be entangled. This generic result places a limit on our ability to observe intrinsic electronic quantum criticality.

The preparation and preservation of entangled quantum states is particularly relevant for the development of quantum computers, where interacting quantum bits (qubits) must produce states sufficiently long lived for meaningful manipulation. The state lifetime, typically referred to as decoherence time, is derived from coupling to the background environment. For solid-state quantum computing schemes, the qubits are typically electron spins, and they couple to two generic background environments (1). The oscillator bath—that is, delocalized environmental modes (2) such as thermal vibrations coupled via magnetoelastic terms to the spins—can be escaped by lowering the temperature to a point where the lattice is essentially

frozen. Coupling to local degrees of freedom, such as nuclear magnetic moments that form a spin bath, may prove more difficult to avoid, because all spin-based candidate materials for quantum computation have at least one naturally occurring isotope that carries nuclear spin.

Experimental work in this area has been largely restricted to the relaxation of single, weakly interacting magnetic moments such as those on large molecules (3); much less is known about spins as they might interact in a real quantum computer. In this regard, the insight that quantum phase transitions (QPTs) (4) are a good arena for looking at fundamental quantum properties of strongly interacting spins turns out to be valuable, as it has already been for explorations of entanglement. In particular, we show that coupling to a nuclear spin bath limits the distance over which quantum mechanical mixing affects the electron spin dynamics.

QPTs are transitions between different ground states driven not by thermal fluctuations but by quantum fluctuations controlled by a parameter such as doping, pressure, or magnetic field (5, 6). Much of the interest in QPTs stems from their importance for understanding materials with unconventional properties, such as heavy fermion systems and high-temperature

<sup>1</sup>Laboratory for Neutron Scattering, ETH-Zürich and Paul Scherrer Institut, 5232 Villigen, Switzerland. <sup>2</sup>James Franck Institute and Department of Physics, University of Chicago, Chicago, IL 60637, USA. <sup>3</sup>Risø National Laboratory, DK-4000 Roskilde, Denmark. <sup>4</sup>Ørsted Laboratory, Niels Bohr Institute fAPG, Universitetsparken 5, 2100 Copenhagen, Denmark. <sup>5</sup>London Centre for Nanotechnology and Department of Physics and Astronomy, University College London, London WC1E 6BT, UK. <sup>6</sup>ISIS, Rutherford Appleton Laboratory, Chilton, Didcot OX11 0QX, UK.

\*To whom correspondence should be addressed. E-mail: henrik.ronnow@psi.ch

The Ho ions in  $\text{LiHoF}_4$  are placed on a tetragonal Scheelite lattice with parameters  $a = 5.175 \text{ \AA}$  and  $c = 10.75 \text{ \AA}$ . The crystal-field ground state is a  $\Gamma_{3,4}$  doublet with only a  $c$  component to the angular momentum and hence can be represented by the  $\sigma^z = \pm 1$  Ising states. A transverse field in the  $a$ - $b$  plane mixes the higher lying states with the ground state; this produces a splitting of the doublet, equivalent to an effective Ising model field. The phase diagram of  $\text{LiHoF}_4$  (Fig. 1A) was determined earlier by susceptibility measurements (10) and displays a zero-field  $T_c$  of 1.53 K and a critical field of  $H_c = 49.5 \text{ kOe}$  in the zero temperature limit. The same measurements confirmed the strong Ising anisotropy, with longitudinal and transverse  $g$  factors differing by a factor of 18 (10). The sudden increase in  $H_c$  below 400 mK was explained by alignment of the Ho nuclear moments through the hyperfine coupling. Corrections to phase diagrams as a result of hyperfine couplings have a long history (18) and were noted for the  $\text{LiREF}_4$  ( $RE = \text{rare earth}$ ) series, of which  $\text{LiHoF}_4$  is a member, more than 20 years ago (19). What is new here is that the application of a transverse field and the use of high-resolution neutron scattering spectroscopy allow us to carefully study the dynamics as we tune through the quantum critical point (QCP).

We measured the magnetic excitation spectrum of  $\text{LiHoF}_4$  with the use of the TAS7 neutron spectrometer at Risø National Laboratory, with an energy resolution (full width at half maximum) of 0.06 to 0.18 meV (20). The transverse field was aligned to better than  $0.35^\circ$ , and the sample was cooled in a dilution refrigerator. At the base temperature of 0.31 K, giving a critical field of 42.4 kOe, the excitation spectrum was mapped out below, at, and above the critical field (Fig. 2). For all fields, a single excitation branch disperses upward from a minimum gap at (2,0,0) toward (1,0,0). From (1,0,0) to (1,0,1), the mode shows little dispersion but appears to broaden. The discontinuity on approaching  $(1,0,1 - \epsilon)$  and  $(1 + \epsilon, 0, 1)$  as  $\epsilon \rightarrow 0$  reflects the anisotropy and long-range nature of the magnetic dipole coupling. However, the most important observation is that the (2,0,0) energy, which is always lower than the calculated single-ion energy ( $\sim 0.39 \text{ meV}$  at 42.4 kOe), shrinks upon increasing the field from 36 to 42.4 kOe and then hardens again at 60 kOe. At this qualitative level, what we see agrees with the mode softening predicted for the simple Ising model in a transverse field. However, it appears that the mode softening is incomplete. At the critical field of 42.4 kOe, the mode retains a finite energy of  $0.24 \pm 0.01 \text{ meV}$ . This result is apparent in Fig. 1B, which shows the gap energy as a function of the external field.

To obtain a quantitative understanding of our experiments, we consider the full rare-earth Hamiltonian, which closely resembles that of

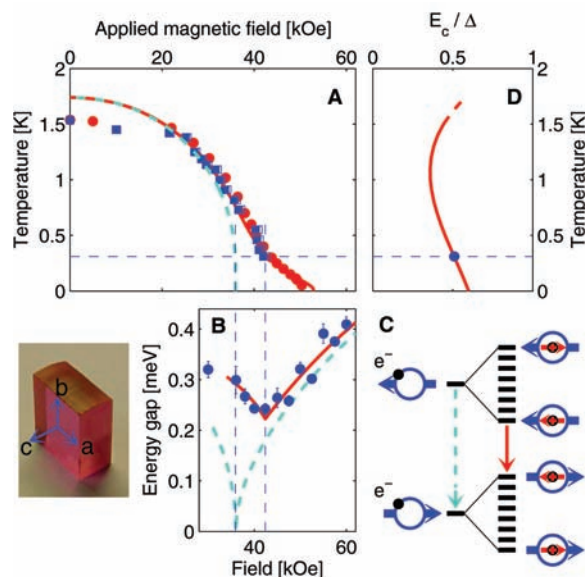
**Fig. 1.** (A) Phase diagram of  $\text{LiHoF}_4$  as a function of transverse magnetic field and temperature from susceptibility ( $\circ$ ) and neutron scattering ( $\square$ ) measurements. Lines are  $1/z$  calculations with (solid) and without (dashed) hyperfine interaction. Horizontal dashed guide marks the temperature 0.31 K at which inelastic neutron measurements were performed. (B) Field dependence of the lowest excitation energy in  $\text{LiHoF}_4$  measured at  $Q = (1 + \epsilon, 0, 1)$ . Lines are calculated energies scaled by  $Z = 1.15$  with (solid) and without (dashed) hyperfine coupling. The dashed vertical guides show how in either case the minimum energy occurs at the field of the transition [compare with (A)]. (C) Schematic of electronic (blue) and nuclear (red) levels as the transverse field is lowered toward the QCP. Neglecting the nuclear spins, the electronic transition (light blue arrow) would soften all the way to zero energy. Hyperfine coupling creates a nondegenerate multiplet around each electronic state. The QCP now occurs when the excited-state multiplet through level repulsion squeezes the collective mode of the ground-state multiplet to zero energy, hence forestalling complete softening of the electronic mode. Of course, the true ground and excited states are collective modes of many Ho ions and should be classified in momentum space. (D) Calculated ratio of the minimum excitation energy  $E_c$  to the single-ion splitting  $\Delta$  at the critical field as a function of temperature. This measures how far the electronic system is from the coherent limit, for which  $E_c/\Delta = 0$ .

Neglecting the nuclear spins, the electronic transition (light blue arrow) would soften all the way to zero energy. Hyperfine coupling creates a nondegenerate multiplet around each electronic state. The QCP now occurs when the excited-state multiplet through level repulsion squeezes the collective mode of the ground-state multiplet to zero energy, hence forestalling complete softening of the electronic mode. Of course, the true ground and excited states are collective modes of many Ho ions and should be classified in momentum space. (D) Calculated ratio of the minimum excitation energy  $E_c$  to the single-ion splitting  $\Delta$  at the critical field as a function of temperature. This measures how far the electronic system is from the coherent limit, for which  $E_c/\Delta = 0$ .

$\text{HoF}_3$  (21, 22). Each Ho ion is subject to the crystal field, the Zeeman coupling, and the hyperfine coupling. The interaction between moments is dominated by the long-range dipole coupling, with a small nearest neighbor exchange interaction  $J_{12}$ :

$$\begin{aligned} \mathcal{H} = & \sum_i [\mathcal{H}_{\text{CF}}(\mathbf{J}_i) + A\mathbf{J}_i \cdot \mathbf{I}_i - g\mu_B\mathbf{J}_i \cdot \mathbf{H}] \\ & - \frac{1}{2} \sum_{ij} \sum_{\alpha\beta} J_D D_{\alpha\beta}(ij) J_{i\alpha} J_{j\beta} \\ & - \frac{1}{2} \sum_{ij}^{n.n.} J_{12} \mathbf{J}_i \cdot \mathbf{J}_j \end{aligned} \quad (2)$$

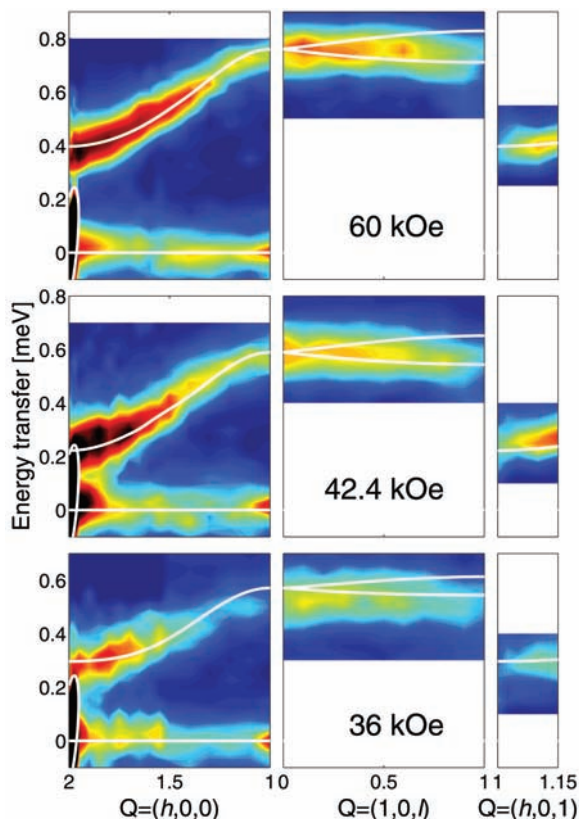
where  $\mathbf{J}$  and  $\mathbf{I}$  are the electronic and nuclear moments, respectively, and for  $^{165}\text{Ho}^{3+}$   $J = 8$  and  $I = 7/2$ . Hyperfine resonance (23) and heat capacity measurements (24) show the hyperfine coupling parameter  $A = 3.36 \text{ } \mu\text{eV}$  as for the isolated ion, with negligible nuclear-quadrupole coupling. The Zeeman term is reduced by the demagnetization field. The normalized dipole tensor  $D_{\alpha\beta}(ij)$  is directly calculable, and the dipole coupling strength  $J_D$  is simply fixed by lattice constants and the magnetic moments of the ions at  $J_D = (g\mu_B)^2 N = 1.1654 \text{ } \mu\text{eV}$ , where  $\mu_B$  is the Bohr magneton. This leaves as free parameters various numbers appearing in the crystal-field Hamiltonian  $\mathcal{H}_{\text{CF}}$  and the exchange constant  $J_{12}$ . The former are determined (25) largely from electron spin resonance for dilute Ho atoms substituted for Y in  $\text{LiYF}_4$ , whereas the latter is constrained



by the phase diagram determined earlier (10) (Fig. 1A). We have used an effective medium theory (9) previously applied to  $\text{HoF}_3$  (26) to fit the phase diagram, and we conclude that a good overall description—except for a modest (14%) overestimate of the zero-field transition temperature—is obtained for  $J_{12} = -0.1 \text{ } \mu\text{eV}$ . On the basis of quantum Monte Carlo simulation data, others (27) have also concluded that  $J_{12}$  is substantially smaller than  $J_D$ .

Having established a good parameterization of the Hamiltonian, we model the dynamics, where expansion to order  $1/z$  (where  $z$  is the number of nearest neighbors of an ion in the lattice) leads to an energy-dependent renormalization  $[1 + \Sigma(\omega)]^{-1}$  (on the order of 10%) of the dynamic susceptibility calculated in the random phase approximation, with the self energy  $\Sigma(\omega)$  evaluated as described in (26). For the three fields investigated in detail, the dispersion measured by neutron scattering is closely reproduced throughout the Brillouin zone. As indicated by the solid lines in Fig. 2, the agreement becomes excellent if the calculated excitation energies are multiplied by a renormalization factor  $Z = 1.15$ . The point is not that the calculation is imperfect but rather that it matches the data as closely as it does. Indeed, it also predicts a weak mode splitting of about  $0.08 \text{ meV}$  at  $(1,0,1 - \epsilon)$ , consistent with the increased width in the measurements. The agreement for the discontinuous jump between  $(1,0,1 - \epsilon)$  and  $(1 + \epsilon, 0, 1)$  as a result of the long-range nature of the dipole coupling shows that this is indeed the dominant coupling.

**Fig. 2.** Pseudocolor representation of the inelastic neutron scattering intensity for  $\text{LiHoF}_4$  at  $T = 0.31$  K observed along the reciprocal space trace  $(2,0,0) \rightarrow (1,0,0) \rightarrow (1,0,1) \rightarrow (1.15,0,1)$ . White lines show the  $1/z$  calculation for the excitation energies as described in the text. White ellipses around the  $(2,0,0)$  Bragg peak indicate 5 times the resolution tail (full width at half maximum).



The simple origin of the incomplete softening and enhanced critical field (Fig. 1, B and C) is easiest to understand if we start from the polarized paramagnetic state above  $H_c$ , where the experiment, the purely electronic calculation, and the theory including the hyperfine coupling all coincide. At high fields, the only effect of the hyperfine term is to split both the ground state and the electronic excitation modes into multiplets that are simply the direct products of the electronic and nuclear levels, with a total span of  $2A(J)I \approx 0.1$  meV (Fig. 1C). Upon lowering the field, the electronic mode softens and would reach zero energy at  $H_c^0 = 36$  kOe in the absence of hyperfine coupling. The hyperfine coupling, however, already mixes the original ground and excited (soft mode) states above  $H_c$ . As this happens, the formation of a composite spin from mixed nuclear and electronic contributions immediately stabilizes ordering along the  $c$  axis of the crystal. In other words, the hyperfine coupling shunts the electronic mode, raising the critical field to the observed  $H_c = 42.4$  kOe, where the mode reaches a nonzero minimum. This process is accompanied by transfer of intensity from the magnetic excitation of electronic origin to soft modes of much lower energy (in the 10- $\mu$ eV range) that have an entangled nuclear/electronic character. Cooling to very low temperatures would reveal these modes as propagating and softening to zero at the QCP, but at the temperatures

reachable in our measurements there is thermalization, dephasing the composite modes to yield the strong quasi-elastic scattering appearing around  $Q = (2,0,0)$  and zero energy at the critical field, as in Fig. 2.

The intensities of the excitations are simply proportional to the matrix elements  $|\langle f | \sum_j \exp(iQ \cdot R_j) J_j^+ | 0 \rangle|^2$ , and therefore provide a direct measure of the wave functions via the interference effects implicit in the spatial Fourier transform of  $J_j$ . Figure 3 shows intensities recorded along  $(h,0,0)$  for the three fields 36, 42.4, and 60 kOe. They follow a momentum dependence characterized by a broad peak near  $(2,0,0)$ , which is well described by our theory. In the absence of hyperfine interactions, the intensity at  $H_c^0$  would diverge as  $q$  approaches  $(2,0,0)$ , reflecting that the real-space dynamical coherence length  $\xi_c$  of the excited state grows to infinity. The finite width of the peak observed at  $H_c$  corresponds in real space to a distance on the order of the interholmium spacing; because the hyperfine interactions forestall the softening of the electronic mode, the implication is that these interactions also limit the distance over which the electronic wave functions can be entangled (4). Thus, Fig. 3 is a direct demonstration of the limitation of quantum coherence in space via coupling to a nuclear spin bath.  $\xi_c$  is obtained from a sum over matrix elements connecting the ground state to a particular set of excited states, whereas the thermodynamic correlation length

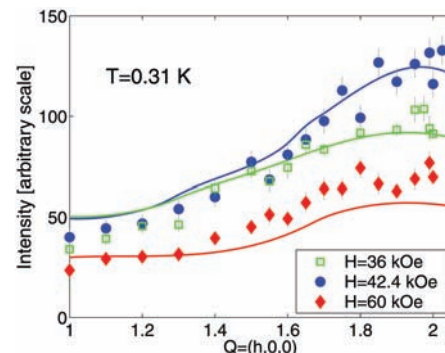


**Fig. 3.** Measured intensities of the excitations along  $Q = (h,0,0)$  at the same values of the field as in Fig. 2. Lines are calculated with geometric and resolution corrections applied to allow comparison to the neutron data.

$\xi_t$  is derived from the equal time correlation function  $S(r)$ , which is the sum over all final states.  $\xi_t$  diverges at second-order transitions such as those in  $\text{LiHoF}_4$ , where the quasielastic component seen in our data dominates the long-distance behavior of  $S(r)$  at  $T_c(H)$ . It is the electronic mode, and hence  $\xi_c$ , that dictates to what extent  $\text{LiHoF}_4$  can be characterized and potentially exploited as a realization of the ideal transverse-field Ising model.

Beyond providing a quantitative understanding of the excitations near the QCP of a model experimental system, we obtain new insight by bringing together the older knowledge from rare-earth magnetism and the contemporary ideas of entanglement, qubits, and decoherence. Although the notion of the spin bath was developed to address decoherence in localized magnetic clusters and molecules (1), our work discloses its importance for QPTs. In particular, we establish that the spin bath is a generic feature that will limit our ability to observe intrinsic electronic quantum criticality. This may not matter much for transition metal oxides with very large exchange constants, but it could matter for rare earth and actinide intermetallic compounds, which show currently unexplained crossovers to novel behaviors at low ( $<1$  K) temperatures [see, e.g., (28)].

For magnetic clusters, decoherence can be minimized in a window between the oscillator bath-dominated high-temperature regions and the spin bath-dominated low-temperature regions (29). Our calculations suggest that the dense quantum critical magnet shows analogous behavior. Here the interacting electron spins themselves constitute the oscillator bath, and the extent to which the magnetic excitation softens at  $T_c(H)$ , as measured by the ratio of the zone center energy  $E_c$  to the field-induced single-ion splitting  $\Delta$  (Fig. 1D), gauges the electronic decoherence.  $E_c/\Delta$  achieves its minimum not at  $T = 0$  but rather at an intermediate temperature  $T \approx 1$  K, exactly where the phase boundary in Fig. 1A begins to be affected by the nuclear hyperfine interactions.



References and Notes

1. N. V. Prokof'ev, P. C. E. Stamp, *Rep. Prog. Phys.* **63**, 669 (2000).
2. R. P. Feynman, F. L. Vernon, *Ann. Phys.* **24**, 118 (1963).
3. W. Wernsdorfer, S. Bhaduri, R. Tiron, D. N. Hendrickson, G. Christou, *Phys. Rev. Lett.* **89**, 197201 (2002).
4. A. Osterloh, L. Amico, G. Falci, R. Fazio, *Nature* **416**, 608 (2002).
5. S. Sachdev, *Phys. World* **12**, 33 (1999).
6. S. Sachdev, *Quantum Phase Transitions* (Cambridge Univ. Press, Cambridge, 1999).
7. P. G. de Gennes, *Solid State Commun.* **1**, 132 (1963).
8. R. J. Elliott, P. Pfeuty, C. Wood, *Phys. Rev. Lett.* **25**, 443 (1970).
9. R. B. Stinchcombe, *J. Phys. C* **6**, 2459 and 2484 (1973).
10. D. Bitko, T. F. Rosenbaum, G. Aeppli, *Phys. Rev. Lett.* **77**, 940 (1997).
11. T. F. Rosenbaum *et al.*, *J. Appl. Phys.* **70**, 5946 (1991).
12. D. Bitko, thesis, University of Chicago (1997).
13. R. Giraud *et al.*, *Phys. Rev. Lett.* **87**, 057203 (2001).
14. J. Brooke, D. Bitko, T. F. Rosenbaum, G. Aeppli, *Science* **284**, 779 (1999).
15. J. Brooke, T. F. Rosenbaum, G. Aeppli, *Nature* **413**, 610 (2001).
16. S. Ghosh, R. Parthasarathy, T. F. Rosenbaum, G. Aeppli, *Science* **296**, 2195 (2002).
17. S. Ghosh *et al.*, *Nature* **425**, 48 (2003).
18. K. Andres, *Phys. Rev. B* **7**, 4295 (1973).
19. R. W. Youngblood, G. Aeppli, J. D. Axe, J. A. Griffin, *Phys. Rev. Lett.* **49**, 1724 (1982).
20. H. M. Rønnow, thesis, Risø National Laboratory, Denmark (2000).
21. M. J. M. Leask *et al.*, *J. Phys. C* **6**, 505 (1994).
22. A. P. Ramirez, J. Jensen, *J. Phys. C* **6**, L215 (1994).
23. J. Magariño, J. Tuchendler, P. Beauvillain, I. Laursen, *Phys. Rev. B* **21**, 18 (1980).
24. G. Mennenga, L. J. de Jongh, W. J. Huiskamp, *J. Magn. Magn. Mater.* **44**, 59 (1984).
25. H. M. Rønnow *et al.*, in preparation.
26. J. Jensen, *Phys. Rev. B* **49**, 11833 (1994).
27. P. B. Chakraborty, P. Henelius, H. Kjønsgberg, A. W. Sandvik, S. M. Girvin, *Phys. Rev. B* **70**, 144411 (2004).
28. P. Gegenwart *et al.*, *Phys. Rev. Lett.* **89**, 056402 (2002).
29. P. C. E. Stamp, I. S. Tupitsyn, *Phys. Rev. B* **69**, 014401 (2004).
30. We thank G. McIntyre for his expert assistance during complementary measurements on the D10 diffractometer at the Institut Laue Langevin, Grenoble, France. Work at the University of Chicago was supported by NSF Materials Research Science and Engineering Centers grant DMR-0213745. Work in London was supported by the Wolfson-Royal Society Research Merit Award Program and the Basic Technologies program of the UK Research Councils.

6 December 2004; accepted 23 February 2005  
10.1126/science.1108317

# Atomic-Scale Visualization of Inertial Dynamics

A. M. Lindenberg,<sup>1</sup> J. Larsson,<sup>2</sup> K. Sokolowski-Tinten,<sup>3</sup>  
K. J. Gaffney,<sup>1</sup> C. Blome,<sup>4</sup> O. Synnergren,<sup>2</sup> J. Sheppard,<sup>5</sup>  
C. Caleman,<sup>6</sup> A. G. MacPhee,<sup>7</sup> D. Weinstein,<sup>7</sup> D. P. Lowney,<sup>7</sup>  
T. K. Allison,<sup>7</sup> T. Matthews,<sup>7</sup> R. W. Falcone,<sup>7</sup> A. L. Cavalieri,<sup>8</sup>  
D. M. Fritz,<sup>8</sup> S. H. Lee,<sup>8</sup> P. H. Bucksbaum,<sup>8</sup> D. A. Reis,<sup>8</sup> J. Rudati,<sup>9</sup>  
P. H. Fuoss,<sup>10</sup> C. C. Kao,<sup>11</sup> D. P. Siddons,<sup>11</sup> R. Pahl,<sup>12</sup>  
J. Als-Nielsen,<sup>13</sup> S. Duesterer,<sup>4</sup> R. Ischebeck,<sup>4</sup> H. Schlarb,<sup>4</sup>  
H. Schulte-Schrepping,<sup>4</sup> Th. Tschentscher,<sup>4</sup> J. Schneider,<sup>4</sup>  
D. von der Linde,<sup>14</sup> O. Hignette,<sup>15</sup> F. Sette,<sup>15</sup> H. N. Chapman,<sup>16</sup>  
R. W. Lee,<sup>16</sup> T. N. Hansen,<sup>2</sup> S. Techert,<sup>17</sup> J. S. Wark,<sup>5</sup> M. Bergh,<sup>6</sup>  
G. Huld,<sup>6</sup> D. van der Spoel,<sup>6</sup> N. Timneanu,<sup>6</sup> J. Hajdu,<sup>6</sup>  
R. A. Akre,<sup>18</sup> E. Bong,<sup>18</sup> P. Krejčík,<sup>18</sup> J. Arthur,<sup>1</sup> S. Brennan,<sup>1</sup>  
K. Luening,<sup>1</sup> J. B. Hastings<sup>1</sup>

The motion of atoms on interatomic potential energy surfaces is fundamental to the dynamics of liquids and solids. An accelerator-based source of femtosecond x-ray pulses allowed us to follow directly atomic displacements on an optically modified energy landscape, leading eventually to the transition from crystalline solid to disordered liquid. We show that, to first order in time, the dynamics are inertial, and we place constraints on the shape and curvature of the transition-state potential energy surface. Our measurements point toward analogies between this nonequilibrium phase transition and the short-time dynamics intrinsic to equilibrium liquids.

In a crystal at room temperature, vibrational excitations, or phonons, only slightly perturb the crystalline order. In contrast, liquids explore a wide range of configurations set by the topology of a complex and time-dependent potential energy surface (1, 2). By using light to trigger changes in this energy landscape, well-defined initial and final states can be generated to which a full range of time-resolved techniques may be applied. In particular, light-induced structural transitions between the crystalline and liquid states of matter may act as simple models for dynamics intrinsic to the liquid state or to transition states in general (3).

In this context, a new class of nonthermal processes governing the ultrafast solid-liquid melting transition has recently emerged,

supported by time-resolved optical (4–7) and x-ray (8–10) experiments and with technological applications ranging from micromachining to eye surgery (11). Intense femtosecond excitation of semiconductor materials results in the excitation of a dense electron-hole plasma, with accompanying dramatic changes in the interatomic potential (12–14). At sufficiently high levels of excitation, it is thought that this process leads to disordering of the crystalline lattice on time scales faster than the time scale for thermal equilibration [often known as the electron-phonon coupling time, on the order of a few picoseconds (15)]. In a pioneering study, Rousse *et al.* (9) determined that the structure of indium antimonide (InSb) changes on sub-picosecond time scales, but the mechanism by which this occurs and the

microscopic pathways the atoms follow have remained elusive, in part because of uncertainties in the pulse duration of laser-plasma sources and signal-to-noise limitations.

Research and development efforts leading toward the Linac Coherent Light Source (LCLS) free-electron laser have facilitated the construction of a new accelerator-based x-ray source, the Sub-Picosecond Pulse Source (SPPS), which uses the same linac-based acceleration and electron bunch compression schemes to be used at future free-electron lasers (16, 17). In order to produce femtosecond x-ray bursts, electron bunches at the Stanford Linear Accelerator Center (SLAC) are chirped and then sent through a series of energy-dispersive magnetic chicanes to create 80-fs electron pulses. These pulses are then transported through an undulator to create sub-100-femtosecond x-ray pulses (18). In order to overcome the intrinsic jitter between x-rays and a Ti:sapphire-based femtosecond laser

<sup>1</sup>Stanford Synchrotron Radiation Laboratory/Stanford Linear Accelerator Center (SLAC), Menlo Park, CA 94025, USA. <sup>2</sup>Department of Physics, Lund Institute of Technology, Post Office Box 118, S-22100, Lund, Sweden. <sup>3</sup>Institut für Optik und Quantenelektronik, Friedrich-Schiller Universität Jena, Max-Wien-Platz 1, 07743 Jena, Germany. <sup>4</sup>Deutsches Elektronen-Synchrotron DESY, Notkestrasse 85, 22607 Hamburg, Germany. <sup>5</sup>Department of Physics, Clarendon Laboratory, Parks Road, University of Oxford, Oxford OX1 3PU, UK. <sup>6</sup>Department of Cell and Molecular Biology, Biomedical Centre, Uppsala University, SE-75124 Uppsala, Sweden. <sup>7</sup>Department of Physics, University of California, Berkeley, CA 94720, USA. <sup>8</sup>FOCUS (Frontiers in Optical Coherent and Ultrafast Science) Center, Department of Physics and Applied Physics Program, University of Michigan, Ann Arbor, MI 48109, USA. <sup>9</sup>Advanced Photon Source, <sup>10</sup>Materials Science Division, Argonne National Laboratory, Argonne, IL 60439, USA. <sup>11</sup>National Synchrotron Light Source, Brookhaven National Laboratory, Upton, NY 11973, USA. <sup>12</sup>Consortium for Advanced Radiation Sources, University of Chicago, Chicago, IL 60637, USA. <sup>13</sup>Niels Bohr Institute, Copenhagen University, 2100 Copenhagen Ø, Denmark. <sup>14</sup>Institut für Experimentelle Physik, Universität Duisburg-Essen, D-45117 Essen, Germany. <sup>15</sup>European Synchrotron Radiation Facility, 38043 Grenoble Cedex 9, France. <sup>16</sup>Physics Department, Lawrence Livermore National Laboratory, Livermore, CA 94550, USA. <sup>17</sup>Max Planck Institute for Biophysical Chemistry, Am Faßberg 11, 37077 Göttingen, Germany. <sup>18</sup>SLAC, Menlo Park, CA 94025, USA.